Cohesive detachment of an elastic pillar from a dissimilar substrate

N. A. Fleck[1,2], S. N. Khaderi[1], R. M. McMeeking[2,3,4], and E. Arzt[2,5]

[1] Cambridge University Engineering Dept., Trumpington St., Cambridge, CB2 1PZ, UK

[2] INM-Leibniz Institute for New Materials, Campus D22, 66123 Saarbruecken, Germany

[3] Departments of Materials and Mechanical Engineering, University of California, Santa Barbara, CA 93106, USA

[4] School of Engineering, University of Aberdeen, King's College, Aberdeen, AB24 2UE, UK

[5] Department of Materials Science and Engineering, Saarland University, Campus D22, Saarbruecken, Germany

Summary

The adhesion of micron-scale surfaces due to intermolecular interactions is a subject of intense interest spanning electronics, biomechanics and the application of soft materials to engineering devices. The degree of adhesion is sensitive to the diameter of micro-pillars in addition to the degree of elastic mismatch between pillar and substrate. Adhesion-strength-controlled detachment of an elastic circular cylinder from a dissimilar substrate is predicted using a Dugdale-type of analysis, with a cohesive zone of uniform tensile strength emanating from the interface corner. Detachment initiates when the opening of the cohesive zone attains a critical value, giving way to crack formation. When the cohesive zone size at crack initiation is small compared to the pillar diameter, the initiation of detachment can be expressed in terms of a critical value H_c of the corner stress intensity. The estimated pull-off force is somewhat sensitive to the choice of stick/slip boundary condition used on the cohesive zone, especially when the substrate material is much stiffer than the pillar material. The analysis can be used to predict the sensitivity of detachment force to the size of pillar and to the degree of elastic mismatch between pillar and substrate.

1. Introduction

Adhesion plays an important role in contact problems at small scale, such as (i) stiction of micro-electromechanical-systems (van Spengen et al. (2002)), (ii) wafer bonding of silicon layers in electronics (Plössl and Kräuter (1999)) and (iii) the adhesion of insects

and animals (such as the gecko) to smooth walls (Arzt et al. (2003)). The mechanics of adhesion falls into two categories: *conforming contacts* such as a sphere on half-space, and *non-conforming contacts* such as a flat-bottomed punch on half-space. We consider each in turn.

Johnson et al. (1971) developed the so-called JKR theory to predict the effect of adhesion upon the Hertzian contact between conforming elastic spheres, with adhesion characterized by a surface energy, which is equivalent to a toughness measure G_c in fracture mechanics. This approach assumes that the process zone size, over which adhesive tractions exist, is much less than the contact size. To assess this, Maugis (1992) developed a cohesive zone model for adhesion and idealised the adhesive traction versus separation law by a constant normal traction σ_c for any separation less than a critical value δ_c. The work of adhesion associated with this cohesive zone law is $G_c = \sigma_c \delta_c$. The length of cohesive zone is of order $\delta_c E^* / \sigma_c$ where E^* is a combined measure of Young's modulus (as defined in (1.2) below). Maugis thereby demonstrated that JKR theory suffices when $\delta_c E^* / \sigma_c$ is a small fraction of the contact width.

The mechanics of *non-conforming* contacts in the presence of adhesion has received much less attention. For example, the adhesion of a flat-ended, *frictionless rigid* pillar on a half-space has been explored for both plane and axisymmetric geometries (Kendall (1971) and Maugis (2000)). These geometries give rise to an inverse square-root singularity in stress at the interface-corner. Consequently, the pull-off force can be obtained by equating the elastic energy release rate of this crack-like singularity to the interfacial work of adhesion, or toughness, G_c. This inverse square-root singularity is relaxed somewhat upon replacing the rigid pillar by a compliant pillar. Adams (2014) has recently explored the problem of a flat-ended, *frictionless compliant* pillar on a half-space made from a dissimilar elastic solid. He assumed that the adhesive traction versus separation law comprises a constant normal traction σ_c for any separation less than a critical value δ_c. The work of adhesion associated with this cohesive zone law is again $G_c = \sigma_c \delta_c$. Adams (2014) assumed that the cohesive zone is sufficiently small that it is embedded within the zone of dominance of the corner singularity. The present study complements this work by considering the case of a compliant pillar

bonded to a dissimilar half-space, and by considering the case where the cohesive zone may occupy a significant fraction of the interface between pillar and substrate.

Our study builds upon the analysis of Khaderi et al. (2015) for the adhesion-energy-controlled detachment of an adhered micropillar from a dissimilar elastic substrate. A flat-bottomed planar pillar of width *D*, or a flat-bottomed circular pillar of diameter *D*, is bonded to a dissimilar half-space, see Fig. 1. The pillar is made from material 1 and the half-space is made from material 2. Both materials are elastic and isotropic, with shear moduli (μ_1, μ_2) and Poisson ratios (ν_1, ν_2). For later use, the elastic mismatch between these two materials is characterized by the two Dundurs' parameters

$$\alpha = \frac{\mu_1(\kappa_2+1)-\mu_2(\kappa_1+1)}{\mu_1(\kappa_2+1)+\mu_2(\kappa_1+1)}, \quad \text{and} \quad \beta = \frac{\mu_1(\kappa_2-1)-\mu_2(\kappa_1-1)}{\mu_1(\kappa_2+1)+\mu_2(\kappa_1+1)}, \tag{1.1}$$

where $\kappa_m = 3-4\nu_m$ for materials *m* =1,2. We shall also make use of the combined modulus E^* as defined by

$$\frac{16}{E^*} = \frac{\kappa_1+1}{\mu_1} + \frac{\kappa_2+1}{\mu_2} \tag{1.2}$$

1.1 Corner singularity between a sticking pillar and substrate

Application of an axial tensile stress σ^∞ to the free end of the bonded pillar results in a singularity in stress at the interface-corner between pillar and substrate, as described by Khaderi et al. (2015). An eigenvalue analysis reveals that the stress field near the corner is dominated by two singular eigenfields having eigenvalues (λ_1, λ_2) with corresponding intensities (H_1, H_2), as follows. Introduce the polar co-ordinates of radius *r* from the corner and angle θ from the interface. Then, the asymptotic stress σ_{ij} and displacement u_j fields in the vicinity of the corner can be written as

$$\sigma_{ij} = H_1 r^{\lambda_1-1} f_{ij}(\lambda_1,\theta) + H_2 r^{\lambda_2-1} f_{ij}(\lambda_2,\theta) \tag{1.3}$$

and

$$u_j = H_1 r^{\lambda_1} g_j(\lambda_1, \theta) + H_2 r^{\lambda_2} g_j(\lambda_2, \theta) \qquad (1.4)$$

in terms of the eigenfunctions f_{ij} and g_j, with higher order terms neglected. The first two eigenvalues (λ_1, λ_2) associated with the leading 2 terms in the infinite series of eigenfunctions both lie within the interval [0.5, 1], and imply unbounded stress as $r \to 0$ whereas the higher terms in the asymptotic series give contributions to σ_{ij} that tend to zero as $r \to 0$. The values of (λ_1, λ_2) depend upon the material mismatch parameters (α, β) as plotted in Fig. 3 of Khaderi et al. (2015). These two eigenvalues are sufficiently close in magnitude that both terms in (1.3) and (1.4) need to be included in the present study. Both eigenvalues are real for the full range of α when $\beta = 0$. When $\beta = \alpha/4$, the eigenvalues (λ_1, λ_2) are real for $\alpha \le 0.86$ and are complex conjugates of each other for $\alpha > 0.86$, see Fig. 3(b) of Khaderi et al. (2015). For benchmarking purposes, when λ_1 equals 0.5, the level of singularity is identical to that of a crack in a homogeneous solid. Analytical expressions exist for the functions f_{ij} and g_j by asymptotic analysis, see for example Knésl and Náhlík (2007), Klusák and Náhlík (2007), Khaderi et al. (2015) and Akisanya and Fleck (1997). The singular zone extends from the corner by approximately 10% of the pillar diameter.

Dimensional arguments dictate that the corner stress intensities (H_1, H_2) are related to the remote stress and geometry according to

$$H_n = \sigma^{\infty} D^{1-\lambda_n} a_n(\alpha, \beta) \ , \quad n = 1,2 \qquad (1.5)$$

where the calibration factors a_n have been reported already by Khaderi et al. (2015) using finite element analysis and a domain integral approach. Note that the values of a_n differ for the plane strain (2D) and axisymmetric (3D) pillars. Assume that the pillar detaches from the substrate by the nucleation of a crack at the pillar-substrate interface. Then, following the argument of Akisanya and Fleck (1997), detachment occurs when the value of the corner stress intensity H_1 attains the critical value H_c, upon neglecting the role of H_2. The material property H_c can be measured by performing experiments for any combination of elastic mismatch. Assume that failure initiates at $H_1 = H_c$. Then, (1.5) gives the sensitivity of pull-off stress σ^{∞} to pillar dimension *D*.

1.2 Micromechanical origins of critical stress intensity H_c

Consider the general problem of a pre-existing corner crack of length c with a cohesive zone of length ℓ at its tip, embedded within an outer singularity in the form of the H_1 field, such that $c+\ell \ll D$, as sketched in Fig. 2. Detachment of the pillar by crack advance is deemed to be either *energy-controlled* or *strength-controlled* depending upon the crack length c in relation to the process zone size at failure ℓ, as follows. Idealise the process zone by a cohesive zone with normal traction of constant strength σ_c up to a critical opening δ_c, and zero strength at greater openings than δ_c. The interfacial toughness, as defined by the area under the traction versus separation curve, follows immediately as $G_c = \sigma_c \delta_c$. Recall that the length of the process zone is only mildly dependent upon the shape of the normal traction versus separation curve, and is given by $\ell = \Lambda E^* G_c / {\sigma_c}^2$, see Wang and Suo (1990). Here, Λ is a dimensionless parameter that depends on mode mix ψ, elastic mismatch and shape of traction versus separation curve; it is typically in the range 0.1 to 0.6. Now assume typical values of adhesion energy, G_c=50 mJ/m^2, and of cohesive strength, σ_c = 0.1 MPa, for a PDMS pillar and substrate (Tang et al., 2005). Then, ℓ is in the range 1 μm to 5 μm. Two detachment mechanisms can now be envisaged, depending upon the ratio ℓ / c, as follows.

(i) **Adhesion-energy-controlled detachment** for $\ell \ll c$. Khaderi et al. (2015) confined their attention to this limit, and obtained an expression for H_c in terms of the interfacial toughness G_c and flaw length *c*, such that

$$H_c = \frac{1}{|d_1|}\left(\frac{E^* G_c}{\left(1-\beta^2\right)c^{2\lambda_1 - 1}}\right)^{1/2} \tag{1.6}$$

by making use of (10)-(13) in Khaderi et al. (2015). The dependence of λ_1 and of the complex coefficient d_1 upon (α, β) is plotted in Figs. 3 and 9, respectively, of Khaderi et al. (2015). Note that λ_1 is in the range 0.5 to 0.7, and so there is only a mild dependence of H_c upon defect length *c*.

(ii) **Adhesion-strength-controlled detachment** for $\ell >> c$. Detachment occurs from the interface of strength σ_c and toughness G_c. *We shall explore strength-controlled detachment in the present study for an axisymmetric cylindrical pillar* and limit our attention to the case of a vanishing initial defect, $c/\ell \to 0$. We shall show below that H_c is given by

$$H_c = k\sigma_c \left(\frac{E^* G_c}{{\sigma_c}^2} \right)^{1-\lambda_1} \tag{1.7}$$

where the parameter *k* depends upon (α, β) and is expressed in terms of various coefficients to be introduced throughout our study, with the form

$$k = \left[N_1 \left(\frac{d_1^R}{f_R} \right)^{\frac{\lambda_1}{1-\lambda_1}} - N_f \left(\frac{d_1^R}{f_R} \right)^{\frac{1}{1-\lambda_1}} \right]^{\lambda_1 - 1} \tag{1.8}$$

The derivations of (1.7) and (1.8) are detailed later in the paper, and all parameters including *k*, as given in (1.8), are listed in Table 1 for selected values of (α, β). The dependence of *k* upon (α, β) is also plotted in Fig. 3, and we note that it takes values in the range 0.4 to 0.8, depending upon (α, β). We emphasise that the present study considers both the limits of a small cohesive zone relative to the pillar diameter (such that the cohesive zone is embedded within the corner singularity), and the more general case of a large cohesive zone that extends over a large fraction of the pillar diameter (beyond the corner singularity).

2. Problem statement

Within the assumptions of linear elasticity theory, and in the absence of a cohesive zone between pillar and half-space, the application of an axial stress to the remote end of the pillar leads to a singularity in stress at the interface corner. Consequently, detachment of the pillar begins at the interface corner; this is commonly observed, see for example Greiner et al. (2007) and Del Campo et al. (2007).

In the present treatment we shall model adhesion-strength-controlled detachment by assuming that a starter defect is absent (*c*=0 in Fig. 2) but the normal traction on the interface

between a pillar and half-space is moderated by the presence of a cohesive zone of constant tensile strength σ_c on the interface. We endow the cohesive zone with *zero shear traction,* such that slip can freely occur between the faces of the cohesive zone, and a normal tensile traction *T* versus opening δ response, such that $T = \sigma_c$ for $0 < \delta < \delta_c$, and *T*=0 for $\delta > \delta_c$. The toughness of the interface is $G_c = \sigma_c \delta_c$. When a remote tensile stress is applied to the pillar, the interfacial tensile stress at the interface corner is limited to σ_c, see Fig. 1b. The length ℓ of the cohesive zone depends upon the magnitude of the remotely applied stress σ^∞, and is influenced by the degree of elastic mismatch between pillar and half-space. The maximum normal and tangential separations of the cohesive zone exist at the interface corner, and are denoted by δ_N and δ_S, respectively. *We shall assume that detachment of the pillar from the half-space initiates when the maximum normal displacement* δ_N *attains the critical value* δ_c.

The pull-off stress required for detachment is calculated by superposition of two problems A and B, following the approach of Dugdale (1960). The cohesive zone is treated as an interfacial crack of length ℓ, with crack face loading and remote loading as follows:

Problem A: a remote tensile stress σ^∞ is applied to the top of the pillar, as shown in Fig. 1c; and

Problem B: A normal traction of magnitude *T* is applied to the faces of the interfacial crack, see Fig. 1d, such that *T*= σ_c for $0 < \delta < \delta_c$, and *T*=0 for $\delta > \delta_c$.

Consider the case where the applied remote tensile stress σ^∞ is much less than the cohesive strength σ_c. Then, the length ℓ of the cohesive zone is much less than the pillar diameter *D*, and the zone is fully embedded within the *H*-field corner singularity for a fully bonded punch on a half-space (with the cohesive zone absent); the corresponding analysis is referred to as the 'short crack' solution. Alternatively, when σ^∞ is comparable in magnitude to σ_c, the cohesive zone extends beyond the domain of the corner singularity, and the corresponding analysis is referred to as the 'long crack' solution. The pull-off stress $\sigma^\infty = \sigma_F$ for the initiation of pillar detachment (at $\delta_N = \delta_c$) is calculated in each regime as a function of the Dundurs' parameters (α, β). We proceed by considering problems A and B in turn.

2.1 Problem A, corner crack under remote tension

An interfacial crack of length ℓ is present at the corner between pillar and half-space, and a remote tensile stress of magnitude σ^{∞} is applied to the pillar. In the following we summarize the results relevant to short and long crack solutions, as taken from Khaderi et al. (2015).

Short crack solution: The asymptotic stress field (1.3) and displacement field (1.4) exist at the interface corner in the absence of a crack. The values of the calibration factor a_n in (1.5), as a function of the (α,β), have been given by Khaderi et al. (2015), and values for a_1 are repeated in Table 1 of the present study. Now embed an interfacial crack of length ℓ within the *H*-dominated zone (see Fig. 1(e)). The interfacial stress intensity factor is represented by the complex quantity K^{∞}, (see for example Hutchinson and Suo (1991)), and the value of K^{∞} is dictated by the magnitude of the *H*-field according to

$$K^{\infty}\ell^{i\varepsilon} = \sum_{n=1,2} H_n \ell^{\lambda_n - \frac{1}{2}} (d_n^R + i d_n^I) \ , \tag{2.1}$$

where ε is the usual oscillatory index that depends on β according to

$$\varepsilon = \frac{1}{2\pi}\log\frac{1-\beta}{1+\beta} \tag{2.2}$$

and the non-dimensional calibration factors (d_n^R, d_n^I) depend on (α,β). These factors have been tabulated by Khaderi et al. (2015), and selected values for (d_1^R, d_1^I) are repeated in Table 1 for subsequent use. The normal crack mouth displacement δ_N^{∞} and tangential displacement δ_S^{∞} can be written in the form

$$\delta_N^{\infty} = \sum_{n=1,2} \frac{H_n}{E^*} \ell^{\lambda_n} N_n(\alpha,\beta), \quad \delta_S^{\infty} = \sum_{n=1,2} \frac{H_n}{E^*} \ell^{\lambda_n} S_n(\alpha,\beta), \tag{2.3}$$

where E^* has already been defined in Eq. (1.2).

The calibration factors (N_n, S_n) are calculated in the present study by finite element simulations using ABAQUS commercial software[1], by following the method of Khaderi et al. (2015), and we list selected values of (d_1^R, d_1^I) in Table 1. The substrate is represented by a circular cylinder of radius and thickness both equal to 40*D*. Numerical experimentation confirmed that these substrate dimensions are sufficiently large to mimic a half-space. The displacement vanishes at the bottom of the substrate and a normal surface traction, of magnitude σ^∞, is applied to the top of the pillar. The pillar and substrate are discretised using elements of type CAX8.

Long crack solution: Now consider an interfacial crack of length ℓ that extends beyond the *H*-dominated region. The stress intensity factor and crack opening are calculated by performing finite element simulations of the entire geometry, see Fig. 1(c). The complex stress intensity factor is represented by K^∞ and is related to the remote stress σ^∞ according to

$$K^\infty \ell^{i\varepsilon} = \sigma^\infty \ell^{1/2}\left[b_R\left(\alpha,\beta,\frac{\ell}{D}\right) + i b_I\left(\alpha,\beta,\frac{\ell}{D}\right)\right], \tag{2.4}$$

where $\left(b_R, b_I\right)$ are calibration factors. The crack mouth displacement can be written as

$$\delta_N^\infty = \frac{\sigma^\infty}{E^*}\ell N_\infty\left(\alpha,\beta,\frac{\ell}{D}\right), \qquad \delta_S^\infty = \frac{\sigma^\infty}{E^*}\ell S_\infty\left(\alpha,\beta,\frac{\ell}{D}\right) \tag{2.5}$$

where the calibration factors $\left(N_\infty, S_\infty\right)$ are also functions of $(\alpha,\beta,\ell/D)$. The calibration factors are calculated by following the computational procedure of Khaderi et al. (2015), with the same finite element details as those described above for the short crack case.

2.2 Problem B, corner crack under crack face loading

Now consider the second problem of crack-face loading. A crack of length ℓ emanates from the interface corner and a normal traction of magnitude σ_c acts on the crack faces as shown in Fig. 1(d). Again, a short crack regime can be identified, such that

[1] Dassault Systems, Simulia Corporation, Providence, Rhode Island, USA. Version 6.11-1 is used to perform the simulations.

$\ell / D << 1$, with geometry as specified in Fig. 1(f). The full geometry, as shown in Fig. 1(d), is needed to analyse the long crack case, for which the crack length ℓ is comparable to the pillar diameter *D*. The complex stress intensity factor is written as

$$K_f \ell^{i\varepsilon} = \sigma_c \ell^{1/2} \left[f_R\left(\alpha, \beta, \frac{\ell}{D}\right) + i f_I\left(\alpha, \beta, \frac{\ell}{D}\right) \right], \tag{2.6}$$

in terms of the calibration factors (f_R, f_I), and the crack mouth displacement reads

$$\delta_N^f = \frac{\sigma_c}{E^*} \ell N_f\left(\alpha, \beta, \frac{\ell}{D}\right), \qquad \delta_S^f = \frac{\sigma_c}{E^*} \ell S_f\left(\alpha, \beta, \frac{\ell}{D}\right) \tag{2.7}$$

in terms of the calibration factors $\left(N_f, S_f\right)$. The calibration factors for long cracks are also evaluated by the procedure of Khaderi et al. (2015). We list the short-crack limits $f_R\left(\frac{\ell}{D} \to 0\right)$, $f_I\left(\frac{\ell}{D} \to 0\right)$ and $N_f\left(\frac{\ell}{D} \to 0\right)$ in Table 1 for selected values of (α, β).

3. Results

We return to the problem of cohesive detachment of the cylindrical pillar. We first obtain the relation between the cohesive zone length ℓ and remote stress. We then calculate the pull-off stress as a function of the cohesive strength σ_c and critical opening displacement δ_c.

3.1 Cohesive zone length ℓ

The stress intensity factor for the corner crack, due to a remote stress σ^∞ and to crack face loading of magnitude σ_c, is given by the net value $K^{NET} \ell^{i\varepsilon} = K^\infty \ell^{i\varepsilon} - K_f \ell^{i\varepsilon}$. Following the usual Dugdale (1960) argument, the length of the cohesive zone is such that the crack tip tensile stress is bounded and $\mathrm{Re}\left[K^{NET} \ell^{i\varepsilon} \right] = 0$.

First, focus on the short crack limit. Upon equating the real part of $K^{\infty}\ell^{i\varepsilon}$ to the real part of $K_f\ell^{i\varepsilon}$ (as expressed by (2.1) and (2.6), respectively) and by using the relation (1.5) for H_n we obtain

$$\frac{\sigma^{\infty}}{\sigma_c}=\left[\sum_{n=1,2}\left(\frac{\ell}{D}\right)^{\lambda_n-1}a_n d_n^R\right]^{-1} f_R \tag{3.1}$$

thereby providing the relation between cohesive zone length ℓ and the remote stress σ^{∞}.

Second, consider the case of a long crack. Upon equating the real part of $K^{\infty}\ell^{i\varepsilon}$ to $K_f\ell^{i\varepsilon}$ (from (2.4) and (2.6), respectively) the relation between applied stress and cohesive length reads

$$\frac{\sigma^{\infty}}{\sigma_c}=\frac{f_R(\ell/D)}{b_R(\ell/D)}. \tag{3.2}$$

The dependence of cohesive zone length upon remote stress is plotted in Fig. 4 for selected values of α, with $\beta=0$ and $\beta=\alpha/4$. The short crack solution is in agreement with the long crack solution for small values of ℓ/D. For a given remote stress σ^{∞}, the cohesive zone size ℓ increases with increasing α and is relatively insensitive to the magnitude of β. In the short crack limit the cohesive zone size ℓ is almost independent of α for $-0.99<\alpha<0$ when $\beta=0$.

3.2 Critical stress intensity H_c for a short cohesive zone

The critical value (1.7) for the stress intensity H_c for a short cohesive zone can now be established. We consider the case where the cohesive zone is fully embedded within the corner singularity as defined by the H_1-field, and neglect the contribution from the less singular H_2-field. Then, (3.1) simplifies to

$$\ell=\left[\frac{d_1^R}{f_R}\frac{H_1}{\sigma_c}\right]^{\frac{1}{1-\lambda_1}} \tag{3.3}$$

and the net crack mouth opening displacement $\delta = \delta_N^{\infty} - \delta_N^{f}$ follows from (2.3a) and (2.7a) as

$$\delta = \frac{\sigma_c}{E^*}\left(\frac{H_1}{\sigma_c}\right)^{\frac{1}{1-\lambda_1}}\left[N_1\left(\frac{d_1^R}{f_R}\right)^{\frac{\lambda_1}{1-\lambda_1}} - N_f\left(\frac{d_1^R}{f_R}\right)^{\frac{1}{1-\lambda_1}} \right] \tag{3.4}$$

Debonding initiates at $H_1 = H_c$ such that $\delta = \delta_c$, and (3.4) can then be re-expressed as (1.7) where *k* is defined by (1.8) and we have made use of the identity $G_c = \sigma_c \delta_c$.

3.3 Pull-off stress σ_F

We proceed to calculate the remote pull-off stress σ_F as a function of the pillar diameter and the Dundurs' parameters (α, β). The net crack mouth opening displacement is $\delta = \delta_N^{\infty} - \delta_N^{f}$. For the case of a short cohesive zone, the expressions (2.3a) and (2.6a) give

$$\delta = \sum_{n=1,2} \frac{H_n}{E^*} \ell^{\lambda_n} N_n - \frac{\sigma_c}{E^*} \ell N_f . \tag{3.5}$$

and further reduction via (1.5) provides

$$\frac{\delta}{D_c} = \frac{\sigma^{\infty}}{\sigma_c}\left[\sum_{n=1,2}\left(\frac{\ell}{D}\right)^{\lambda_n} a_n N_n \right] - \frac{\ell}{D} N_f , \tag{3.6}$$

where the characteristic diameter D_c is defined as $D_c \equiv \sigma_c D / E^*$. Now use the relation (3.1) between σ^{∞}/σ_c and ℓ / D to obtain

$$\frac{\delta}{D_c} = f_R\left[\sum_{n=1,2}\left(\frac{\ell}{D}\right)^{\lambda_n - 1} a_n d_n^R \right]^{-1}\left[\sum_{n=1,2}\left(\frac{\ell}{D}\right)^{\lambda_n} a_n N_n \right] - \frac{\ell}{D} N_f , \tag{3.7}$$

The expressions (3.1) and (3.7) provide the relation between δ / D_c and σ^{∞}/σ_c as parameterized by ℓ / D.

For long cracks, the crack mouth opening displacement $\delta = \delta_N^{\infty} - \delta_N^{f}$ is

$$\frac{\delta}{D_c} = \frac{\ell}{D}\left[\frac{\sigma^{\infty}}{\sigma_c} N_{\infty} - N_f\right] = \frac{\ell}{D}\left[\frac{f_R}{b_R} N_{\infty} - N_f\right], \tag{3.8}$$

via (2.5a), (2.7a) and (3.2). The expressions (3.2) and (3.8) provide the relation between δ / D_c and $\sigma^{\infty} / \sigma_c$ in terms of the intrinsic variable ℓ / D.

Now assume that adhesion-strength-controlled detachment takes place when the crack mouth opening displacement δ attains a critical value δ_c. Write the remote pull-off stress σ^{∞} as σ_F. We proceed to plot in Fig. 5 the remote pull-off stress σ_F / σ_c as a function of D_c / δ_c for both short and long cracks by making use of (3.7) and (3.1) for short cohesive zones, and (3.8) and (3.2) for long cohesive zones. Results are shown for selected values of α, with $\beta = 0$ and $\beta = \alpha / 4$. In general, the pull-off stress increases with decreasing D_c / δ_c. For small values of D_c / δ_c, that is for $D_c / \delta_c < 10$, the pull-off stress attains the limiting value $\sigma_F \to \sigma_c$. In contrast, for larger values of D_c / δ_c, the pull-off stress decreases with an increase in the normalized diameter. For a given value of D_c / δ_c, the pull-off stress decreases with increasing α.

The case $\alpha = -0.99$*:* Let us focus on the case $\alpha = -0.99$ (i.e. the substrate material 2 is much stiffer than the pillar material 1). Consider the regime where the remote axial failure stress attains the limiting value $\sigma_F \to \sigma_c$ and the cohesive zone length ℓ approaches $D/2$ in Fig 4. We can gain some insight into this limiting case as follows. Note that the stress state within an elastic, frictionless pillar on a rigid substrate with $\ell = D/2$ is identical to that in a pillar under uniform uniaxial tension. In fact, this same solution exists for all values of crack mouth displacement δ provided the crack opening displacement is uniform over the crack face for a crack of length $\ell = D/2$.

The detachment of an elastic pillar from a rigid substrate ($\alpha = -1$) has been analysed previously by Tang et al. (2005) using a cohesive zone analysis, with sliding prevented within the cohesive zone. Contrary to our results of Fig. 5, they find that D_c / δ_c vanishes as

$\sigma_F \to \sigma_c$. In order to confirm that the difference in responses is a consequence of the different boundary conditions, we have performed additional simulations for problem A and B, but now assuming no sliding of the crack faces. The predictions are included in Fig. 6: for $\alpha = -0.99$, we find that D_c / δ_c vanishes for $\sigma_F / \sigma_c \to 1$, in agreement with the findings of Tang et al. (2005). It is clear that that the pull-off stress is somewhat sensitive to the choice of stick/slip boundary condition at small D_c / δ_c.

The case $\alpha = 1$ *and* $\ell << D$*:* An analytical solution relating the interfacial adhesion energy to the pull-off stress has been given by Kendall (1971), when the pillar is rigid and *frictionless*, and the substrate is compliant ($\alpha = 1$). He noted that the corner singularity in the substrate, adjacent to the edge of the punch, is the same as that for a mode I crack, regardless of the presence or absence of a small corner defect ($\ell << D$), and the energy release rate reads

$$G = \frac{\pi}{16} \frac{1-\nu_2^2}{E_2} D\sigma^{\infty 2} \tag{3.9}$$

Upon equating the energy release rate to the interfacial toughness $G = G_c = \sigma_c \delta_c$, (3.9) can be rearranged to the form

$$\frac{\delta_c E^*}{\sigma_c D} = \frac{\pi}{8} \left(\frac{\sigma^\infty}{\sigma_c} \right)^2 . \tag{3.10}$$

Our results in Fig. 5 for the short crack limit of the frictionless pillar at $\alpha = 0.99$ are in very close agreement with this analytic solution for $\alpha = 1$: the curves coincide to within the thickness of the line, and consequently the comparison is not given in Fig. 5.

4. Analytic solution for a rigid, frictionless axisymmetric pillar adhering to an elastic half space with Dugdale zone ($\alpha = 1$ *and finite* ℓ / D)

We proceed to extend the Kendall (1971) solution for the the detachment of a *rigid, frictionless* cylindrical flat-bottomed pillar of radius *R=D*/2 adhered to an isotropic linear elastic half-space with Young's modulus *E* and Poisson's ratio ν. And, we remove the

restriction that $\ell << D$. Assume that a Dugdale cohesive zone, of strength σ_c and normal separation (i.e. interaction distance) δ exists at the corner edge of the pillar. At low values of tensile load *P* applied to the pillar, a Dugdale cohesive zone (of strength σ_c) exists over the annulus $a \le r \le R$, all measured from the axis of the pillar, see Fig. 7a. The length of Dugdale zone is $\ell = R - a$ and the opening profile of the cohesive zone increases from $\delta = 0$ at *r*=*a* to $\delta(R) \le \delta_c$. With increasing load *P*, the Dugdale zone spreads as its inner radius *a* diminishes; and its separation increases until the pull-off force P_c is attained at $\delta(R) = \delta_c$. We shall show below that detachment ensues under decreasing applied force $P < P_c$, such that the cohesive zone migrates over the annulus $a \le r \le b$ where $b < R$, see Fig. 7b. The annulus shrinks inwards such that both *a* and *b* decrease in value (along with *P*) as detachment proceeds. An analytical treatment is now developed to quantify this behaviour. Detachment occurs in two phases as follows.

Phase (i): initial stable detachment under increasing load such that the cohesive zone extends from *r*=*a* to *r*=*b*=*R*, with $\delta(a) = 0$ and $\delta(R) < \delta_c$, followed by

Phase (ii): unstable detachment under decreasing load, such that the cohesive zone extends from *r*=*a* to *r*=*b*<*R*, with $\delta(a) = 0$ and $\delta(b) = \delta_c$.

Fundamental solution

In order to analyse each phase, we need the fundamental solution for a rigid, frictionless pillar subjected to an axial tensile force *P*, adhered to a half-space over $0 \le r \le a$, with a Dugdale cohesive zone of strength σ_c over the outer annulus $a \le r \le b$. This solution is now given, and then applied to each phase of detachment.

The stress intensity factor at radius *a* due to an applied load *P* (see Tada et al. (2000)) is

$$K_I^P = \frac{P\sqrt{\pi a}}{2\pi a^2} \tag{4.1}$$

while the crack opening displacement caused by it (Johnson (1985)) is

$$\delta^P(r) = \frac{P}{\pi a E'} \arccos(a/r) \tag{4.2}$$

where $E' = E/(1-\nu^2)$. The stress intensity factor at radius *a* due to the traction σ_c over the cohesive zone (see Tada *et al*. (2000)) is

$$K_I^C = -\frac{\pi\sigma_c}{(\pi a)^{3/2}}\left(b^2 \arccos(a/b) + a\sqrt{b^2 - a^2}\right) \tag{4.3}$$

Since the total stress intensity factor at radius *a* must be zero, we add Eq. (4.1) and (4.3) and set the result to zero, to give

$$\frac{P}{2b^2\sigma_c} = \arccos(a/b) + (a/b)\sqrt{1-(a/b)^2} \tag{4.4}$$

The crack opening at *r* = *b* due to the applied load *P* as specified in (4.4) is

$$\frac{\pi E'\delta^P(b)}{2b\sigma_c} = (b/a)\arccos^2(a/b) + \arccos(a/b)\sqrt{1-(a/b)^2} \tag{4.5}$$

It remains to determine the crack opening displacement at *r* = *b* due to the traction σ_c over the cohesive zone. We follow the Bueckner/Rice weight function approach and first note that the potential energy for a system with two applied loads, F_1 and F_2, is given by

$$\Psi = -\frac{1}{2}C_{11}{F_1}^2 - C_{12}F_1F_2 - \frac{1}{2}C_{22}{F_2}^2 \tag{4.6}$$

where C_{ij} is the compliance matrix, such that

$$u_1 = -\frac{\partial\Psi}{\partial F_1} = C_{11}F_1 + C_{12}F_2 \tag{4.7}$$

is the coaxial displacement where F_1 is applied and

$$u_2 = -\frac{\partial\Psi}{\partial F_2} = C_{12}F_1 + C_{22}F_2 \tag{4.8}$$

is the coaxial displacement where F_2 is applied, where we bear in mind the fact that the pillar is rigid. (We shall later assume that the forces F_1 and F_2 are point forces applied to the surface of the half-space at 2 locations within the cohesive zone).

For an axisymmetric ligament of radius *a*, the energy release rate is given by

$$G = \frac{1}{2\pi a}\frac{\partial \Psi}{\partial a} = -\frac{1}{4\pi a}\frac{dC_{11}}{da}F_1{}^2 - \frac{1}{2\pi a}\frac{dC_{12}}{da}F_1F_2 - \frac{1}{4\pi a}\frac{dC_{22}}{da}F_2{}^2 \qquad (4.9)$$

Due the Irwin relationship we find that

$$G = \frac{1}{2E'}\left(k_1F_1 + k_2F_2\right)^2 \qquad (4.10)$$

where the factor of 2 in the denominator arises from the fact that the pillar is rigid, k_1 is the stress intensity factor due to unit load applied at location 1, and k_2 is the stress intensity factor due to unit load applied at location 2. Upon matching terms with common factors we find that

$$\frac{dC_{12}}{da} = -\frac{2\pi a k_1 k_2}{E'} \qquad (4.11)$$

where C_{12} is the displacement at location 1 due to a unit load applied at location 2 and *vice versa*. From Tada *et al.* (2000) we find that

$$k_1 = \frac{1}{(\pi a)^{3/2}}\left(\arccos\frac{a}{r} + \frac{a}{\sqrt{r^2 - a^2}}\right) \qquad (4.12)$$

for a unit load applied at *r* on the crack surface and

$$k_2 = \frac{1}{(\pi a)^{3/2}}\left(\arccos\frac{a}{r'} + \frac{a}{\sqrt{r'^2 - a^2}}\right) \qquad (4.13)$$

for a unit load applied on the crack surface at $r¢$. Thus

$$\frac{dC_{12}}{da} = -\frac{2}{E'(\pi a)^2}\left(\arccos\frac{a}{r} + \frac{a}{\sqrt{r^2 - a^2}}\right)\left(\arccos\frac{a}{r'} + \frac{a}{\sqrt{r'^2 - a^2}}\right) \qquad (4.14)$$

where C_{12} is now the crack opening at r due to a unit load on the crack surface applied at r' and *vice versa*. Now integrate (4.14), subject to C_{12} being zero at the smaller of $a = r$ and $a = r'$ since the crack opening at the crack tip is zero and a unit load on the crack surface applied at the crack tip causes zero crack opening. Thus,

$$C_{12} = -\frac{2}{\pi^2 E'} \int_{\min(r,\, r')}^{a} \frac{1}{a'^2} \left(\arccos\frac{a'}{r} + \frac{a'}{\sqrt{r^2 - a'^2}} \right) \left(\arccos\frac{a'}{r'} + \frac{a'}{\sqrt{r'^2 - a'^2}} \right) da' \quad (4.15)$$

Consider cohesive tractions applied in the range $a \le r' \le b$. It follows that the crack opening at r is

$$\delta^C(r) = -\frac{4\sigma_c}{\pi E'} \int_a^b r' \int_a^{\min(r,\, r')} \frac{1}{a'^2} \left(\arccos\frac{a'}{r} + \frac{a'}{\sqrt{r^2 - a'^2}} \right) \left(\arccos\frac{a'}{r'} + \frac{a'}{\sqrt{r'^2 - a'^2}} \right) da' dr' \quad (4.16)$$

Interchanging the order of integration, we obtain

$$\delta^C(r) = -\frac{4\sigma_c}{\pi E'} \int_a^r \frac{1}{a'^2} \left(\arccos\frac{a'}{r} + \frac{a'}{\sqrt{r^2 - a'^2}} \right) \int_{a'}^b \left(r' \arccos\frac{a'}{r'} + \frac{r'a'}{\sqrt{r'^2 - a'^2}} \right) dr' da' \quad (4.17)$$

And, upon integration, this becomes

$$\delta^C(r) = -\frac{2\sigma_c}{\pi E'} \int_a^r \frac{1}{a'^2} \left(\arccos\frac{a'}{r} + \frac{a'}{\sqrt{r^2 - a'^2}} \right) \left(b^2 \arccos\frac{a'}{b} + a'\sqrt{b^2 - a'^2} \right) da' \quad (4.18)$$

Therefore, at $r = b$ we have

$$\delta^C(b) = -\frac{2\sigma_c}{\pi E'} \int_a^b \frac{1}{a'^2} \left(\arccos\frac{a'}{b} + \frac{a'}{\sqrt{b^2 - a'^2}} \right) \left(b^2 \arccos\frac{a'}{b} + a'\sqrt{b^2 - a'^2} \right) da' \quad (4.19)$$

which can be restated as

$$\frac{\pi E'\delta^C(b)}{2\sigma_c b} = -\int_{a/b}^{1} \frac{1}{x^2}\left(\arccos x + \frac{x}{\sqrt{1-x^2}}\right)\left(\arccos x + x\sqrt{1-x^2}\right)dx$$
$$= 2\left(\frac{a}{b}-1\right) + \sqrt{1-\left(\frac{a}{b}\right)^2}\arccos\frac{a}{b} - \frac{b}{a}\arccos^2\frac{a}{b} \tag{4.20}$$

The latter result is used by Maugis et al. (1976). We now combine Eq. (4.5) and (4.20) to obtain the total crack opening at *b* as

$$\frac{\pi E'\delta(b)}{4b\sigma_c} = \left(\frac{a}{b}-1\right) + \sqrt{1-\left(\frac{a}{b}\right)^2}\arccos\frac{a}{b} \tag{4.21}$$

Taken together, Eq. (4.4) and (4.21) are a parameterized load versus deflection curve where the crack opening displacement at *b* is the deflection, and the independent parameter is *a/b*.

Application of solution to phase (i) of detachment

Consider a rigid pillar of radius *R=D/2* subjected to a sufficiently small load *P* that the cohesive zone over the annulus *r=a* to *r=b=R* satisfies $\delta(R) < \delta_c$. The load and displacement now read

$$\frac{P}{2R^2\sigma_c} = \arccos\frac{a}{R} + \frac{a}{R}\sqrt{1-\left(\frac{a}{R}\right)^2} \tag{4.22}$$

from (4.4) and

$$\frac{\pi E'\delta(R)}{4R\sigma_c} = \left(\frac{a}{R}-1\right) + \sqrt{1-\left(\frac{a}{R}\right)^2}\arccos\frac{a}{R} \tag{4.23}$$

from (4.21). Subject to $\delta(R) \le \delta_c$, these results are valid up to a load as given by Eq. (4.22) such that a/R satisfies (4.23) with $\delta(R) = \delta_c$.

Application of solution to phase (ii) of detachment

We proceed to obtain the solution for $\delta(R) > \delta_c$. The cohesive zone now exists over the domain $r=a$ to $r=b<R$, with $\delta(a) = 0$ and $\delta(b) = \delta_c$. We return to Eq. (4.20) and set $\delta(b) = \delta_c$ to obtain

$$\frac{\pi E' \delta_c}{4\sigma_c} = a - b + \sqrt{b^2 - a^2} \arccos\frac{a}{b} \tag{4.24}$$

This gives a relationship between a and b, so that, implicitly, one can be eliminated in favour of the other and the result inserted into Eq. (4.4) to determine the load as a function of the remaining variable.

We now determine whether detachment is unstable under monotonically increasing load, P. To study this, we first observe that the left hand side of Eq. (4.24) is constant if the fibril is being detached and thus b is diminishing. As a consequence, we deduce that during this process

$$\frac{da}{db} = \frac{b}{a}\left[1 - \frac{\left(1-(a/b)\right)\sqrt{1-(a/b)^2}}{\arccos(a/b)}\right] \tag{4.25}$$

Now evaluate dP/db from (4.4)

$$\frac{1}{4b\sigma_c}\frac{dP}{db} = \arccos(a/b) + \frac{a/b}{\sqrt{1-(a/b)^2}} - \frac{a^2/b^2}{\sqrt{1-(a/b)^2}}\frac{da}{db} \tag{4.26}$$

We substitute Eq. (4.25) into this and obtain

$$\frac{\arccos(a/b)}{4b\sigma_c}\frac{dP}{db} = \arccos^2(a/b) + (a/b) - (a/b)^2 \tag{4.27}$$

The right hand side of (4.27) is always positive, and the coefficient of the derivative on the left hand side is also positive. Therefore $dP/db > 0$ and when b diminishes so must P. Therefore detachment occurs under monotonically decreasing load with the detachment force given by Eq. (4.4) subject to $b=R$, $\delta(R) = \delta_c$ and to satisfaction of Eq. (4.24).

We can obtain a plot of the pull-off force as a function of δ_c by cross-plotting Eq. (4.4) and Eq. (4.23), upon taking $\delta(R)=\delta_c$. This plot has been added as a dotted line to Fig. 5a to compare with the finite element prediction for an almost rigid pillar ($\alpha=0.99$); excellent agreement is noted. The length of cohesive zone $\ell=R-a$ as a function of applied force up to the point of detachment is likewise obtained by plotting Eq. (4.4), upon taking $b=R$. Again, the agreement with numerical simulations for $\alpha=0.99$ is excellent, see Fig. 4a.

Concluding Discussion

The present study highlights the significance of the corner singularity in promoting detachment at a pillar-substrate interface. This is confirmed by experiments with artificial patterned surfaces, see for example Del Campo et al. (2007). Mushroom-shaped caps reduce the magnitude of the corner stress intensity H_1 and thereby inhibit detachment. This has recently been analysed in some depth by Balijepalli et al. (2016a).

The cohesion model of the present study highlights the significance of both detachment strength σ_c and adhesion energy G_c in the process of detachment. The detachment stress is dictated by either σ_c or G_c as follows. Consider the two limiting cases:

Case (i): For fibrils of sufficiently small diameter, such that $\sigma_c^{\,2}D/E^*G_c<<3$, the cohesive zone spans the fibril, and the axial strength for fibril detachment σ_F equals σ_c, recall the curves shown in Figs. 5 and 6.

Case (ii): At $\sigma_F/\sigma_c<<1$, the cohesive zone is sufficiently short that it is embedded within the so-called *H*-field of the corner singularity. Assume that, at the onset of detachment, a corner flaw of length *c*, and its cohesive zone of length ℓ are both embedded within the *H*-field. Recall that detachment is adhesion-energy-controlled when $\ell<<c$ and is adhesion-strength-controlled when $\ell<<c$. Also note that the level of singularity λ_1 lies in the range of 0.5 to 0.6, depending upon the values of (α,β), see Fig. 3 of Khaderi et al. (2015). We shall now show that the magnitude of H_c for energy-controlled detachment almost equals that for strength-controlled detachment when $\lambda_1=1/2$. The criterion (1.6) for energy-

controlled detachment implies that H_c scales with $\left(E^* G_c\right)^{1/2}$ and is independent of flaw size c and of cohesive strength σ_c. Likewise, for $\lambda_1 = 1/2$, the criterion (1.7) for strength-controlled detachment implies that H_c scales with $\left(E^* G_c\right)^{1/2}$, where $G_c = \sigma_c \delta_c$. Thus, the difference between the criteria for energy-controlled detachment and for strength-controlled detachment is minor, and is dictated by the magnitude of $\left(E^* G_c\right)^{1/2}$ on the interface, for the case where the cohesive zone length is small compared to the pillar diameter at the onset of detachment. The sensitivity of detachment strength to fibril diameter has been explored previously by Gao et al. (2005) in the context of hierarchical structures in geckos, and the influence of their sizes on adhesion strength.

The exception, in which the trend of increasing strength with diameter reduction is not followed, is that of a compliant fibril on a rigid surface, i.e. when $\alpha = -0.99$, with friction-free cohesion, as can be seen in Fig. 5. In this case the strength rises as the fibril diameter reduces when the strength is low, but then the trend reverses and the asymptotic limit of full cohesive strength is reached only by the diameter increasing again. It is perhaps easier to understand this phenomenon through the fact that the trend is equally driven by the critical interaction distance δ_c increasing. The implication is that for $\delta_c \geq \sigma_c D / \left(10E^*\right)$ we did not find a solution that enables the fibril to remain attached to the substrate until the separation at its perimeter, $\delta\left(D/2\right)$, reaches the critical interaction distance δ_c. That is, before $\delta\left(D/2\right)$ increases to the value δ_c, the whole bottom surface of the fibril acquires a separation $\delta > 0$, and thus the traction applied to the fibril everywhere is equal to σ_c. We deduce from this that, in a solution we did not find numerically, detachment occurs at $\sigma_F = \sigma_c$ for the cases where $\delta_c \geq \sigma_c D / \left(10E^*\right)$. Furthermore, we note that, for $\sigma_c D / \left(E^* \delta_c\right) \geq 10$, there are 2 solutions for the detachment strength, one of which is $\sigma_F = \sigma_c$ and one of which is lower. The solution for which $\sigma_F = \sigma_c$ is certainly the jump-into-contact condition that occurs when the fibril is brought towards the rigid surface. Our solutions indicate that when the fibril is compliant and the substrate is rigid, the lack of friction in the cohesive zone enables the jump-on behaviour also to be a detachment condition. As noted above, sticking conditions in the cohesive zone precludes this behaviour, as is illustrated in Fig. 6.

It is also clear from the present study that the detachment strength for both energy-controlled and strength-controlled detachment is increased by making the pillar from a more compliant material than that of substrate. This points to the use of a compliant layer on the end of the pillar, but the significance of this modification to the pillar awaits a full analysis. Some work on this has been carried out recently by Balijepalli et al. (2016b) and Fischer et al. (2016), but there the enhancement of adhesion associated with a soft tip layer is attributed to the stress distribution induced by the constraint of the stiff stalk on the compliant material. Our results in the present paper suggest that the high compliance of the tip material can have a beneficial effect on adhesion in addition to any stress redistribution achieved.

An interesting feature of our results is that when we consider a rigid fibril adhered to a compliant half-space (i.e $\alpha = 0.99$) with friction-free conditions everywhere at the tip of the fibril, the strength predicted in this case is identical to that computed for the case where the fully adhered region of the fibril tip is subject to sticking friction. It is known that the strength in friction-free conditions is not always the same as that achieved when sticking friction prevails. A case in point is the compliant fibril on a rigid substrate (i.e. $\alpha = -0.99$), where stress in the fibril is uniform in friction-free conditions and thus detachment occurs always at $\sigma_F = \sigma_c$, in contrast to the results in Figs. 4 and 5. However, the fact that the friction-free and sticking friction cases have identical detachment strength when $\alpha = 0.99$ suggests that there is a range of situations in which the friction-free model can be used to gain insights into detachment strength more generally. This is a useful inference as the friction-free case is often easier to analyse, and many of the standard fracture-mechanics results for cracks can be utilised immediately to obtain relevant results.

Acknowledgements

NAF is grateful for financial support in the form of an ERC MULTILAT grant 669764, and to the US ONR (N62909-14-1-N232, project manager, Dr. Dave Shifler). NAF and RMcM acknowledge support from the Alexander von Humboldt Foundation in the form of their *Forschungspreise*, which enabled them to undertake research at INM-Leibniz Institute for New Materials, Saarbrücken. EA acknowledges funding from the European Research Council under the European Union's Seventh Framework Programme (FP/2007-2013) / ERC Grant Agreement n. 340929.

5. References

Adams, G.G. (2014). Adhesion and pull-off force of an elastic indenter from an elastic half-space. *Proc. R. Soc. Lond. A* **470**, 20140317 (doi: 10.1098/rspa.2014.0317).

Akisanya, A., Fleck, N.A. (1997). Interfacial cracking from the free edge of a long bi-material strip. *International Journal of Solids and Structures* **34** (13), 1645–1665.

Arzt, E., Gorb, S., Spolenak, R. (2003). From micro to nano contacts in biological attachment devices. *Proc. Nat. Acad. Sci. USA*, 100, 10603-10606.

Balijepalli, R.G., Begley, M.R., McMeeking, R.M., Fleck, N.A., Arzt, E. (2016a). Numerical simulation of stress singularity and adhesion strength for a compliant mushroom fibril attached to a rigid substrate. *Int. J. Solids and Structs*., **85–86**, 160–171.

Balijepalli, R.G., Fischer, S.C.L., Hensel, R., McMeeking, R.M., Arzt, E. (2016b). Numerical Study of Adhesion Enhancement by Composite Fibrils with Soft Tip Layers. *J. Mech. Phys. Solids*, DOI: 10.1016/j.jmps.2016.11.017 *(in press).*

Del Campo, A., Greiner, C., Arzt, E. (2007). Contact shape controls adhesion of bioinspired fibrillar surfaces. *Langmuir*: **23**, 10235-10243.

Dugdale, D.S. (1960). Yielding of steel sheets containing slits. *J. Mech. Phys. Solids*, **8**, 100-104.

Fischer, S.C.L. , Arzt, E. and Hensel, R. (2016). Composite pillars with tuneable interface for adhesion to rough substrates. *ACS Appl. Mater. Interfaces* (*under revision*).

Gao, H., Wang, X., Yao, H., Gorb, S., Arzt, E. (2005). Mechanics of hierarchical adhesion structures of geckos. *Mech. Mater.* **37**, 275-285.

Greiner C., del Campo, A., Arzt, E. (2007). Adhesion of bioinspired micropatterned surfaces: Effects of pillar radius, aspect ratio, and preload. *Langmuir*, **23**, 3495-3502.

Hutchinson, J.W. and Suo, Z., (1991). Mixed mode cracking in layered materials. *Advances in Applied Mechanics*, ed. J. W. Hutchinson and T. Y. Wu, Academic Press, New York, **29**, 63-191.

Johnson, K. L. (1985). Contact mechanics, Cambridge University Press, ISBN:9781139171731.

Johnson, K. L., Kendall, K., Roberts, A. D. (1971). Surface energy and the contact of elastic solids. *Proc. R. Soc. Lond. A* **324**, 301–313. (doi:10.1098/rspa.1971.0141)

Kendall, K. (1971). The adhesion and surface energy of elastic solids. Journal of Physics D: Applied Physics, **4**(8): 1186-1195.

Khaderi, S.N., Fleck, N.A., Arzt, E., McMeeking, R.M. (2015). Detachment of an adhered micropillar from a dissimilar substrate. *J. Mech. Phys. Solids*, **75**, 159-183.

Klusák, J., Náhlík,L. (2007). Crack initiation criteria for singular stress concentrations, part I: a universal assessment of singular stress concentrations. Eng. Mech. **14**(6), 399–408.

Knésl, Z., Náhlík, L. (2007). Crack initiation criteria for singular stress concentrations, part II: stability of sharp and bi-material notches. Eng. Mech. **14**(6), 409–422.

Maugis, D. (1992). Adhesion of spheres: the JKR-DMT transition using a Dugdale model.

J. Colloid Interface Sci. **150**, 243–269. (doi:10.1016/0021-9797(92)90285-T)

Maugis, D. (2000). *Contact, adhesion and rupture of elastic solids*. Berlin, Germany: Springer.

Maugis, D., Barquins, M., Courtel, R. (1976). Griffith's crack and adhesion of elastic bodies. *Métaux, Corrosion Industries*, **605**, 1-10.

Plössl, A., Kräuter, G. (1999). Wafer direct bonding: tailoring adhesion between brittle materials. *Materials Science and Engineering* **25** (1-2), 1–88.

Tada, H., Paris, P. C., Irwin, G.R. (2000). The Stress Analysis of Cracks Handbook, 3rd edn. ASME Press, New York.

Tang, T., Hui, C.-Y., Glassmaker, N. J., 2005. Can a fibrillar interface be stronger and tougher than a non-fibrillar one? *Journal of The Royal Society Interface* **2**(5), 505–516.

van Spengen, W.M., Puers, R., De Wolf, I.(2002). A physical model to predict stiction in MEMS. *J. Micromech. Microeng*. **12**, 702–713.

Wang, J.S., Suo, Z. (1990). Experimental determination of interfacial toughness curves using Brazil-nut-sandwiches. *Acta. Metall. Mater*. **38,** 1279-1290.

Table 1: Values of various parameters used for evaluating equation 1.8 for selected values of α

(a) $\beta = 0$

α	a_1	λ_1	d_1^R	d_1^I	N_1	S_1	$f_R\left(\frac{\ell}{D}\to 0\right)$	$f_I\left(\frac{\ell}{D}\to 0\right)$	N_f	S_f	k
-0.99	0.278	0.594	2.608	0.789	9.217	1.652	1.882	-0.328	5.255	1.874	0.630
-0.80	0.254	0.584	2.617	0.835	9.194	1.877	1.867	-0.308	5.051	1.728	0.601
-0.60	0.231	0.574	2.623	0.888	9.152	2.125	1.848	-0.283	4.824	1.567	0.573
-0.40	0.208	0.564	2.626	0.943	9.093	2.381	1.829	-0.257	4.591	1.401	0.547
-0.20	0.186	0.554	2.908	0.938	9.016	2.646	1.987	-0.364	4.349	1.228	0.524
0.00	0.157	0.545	2.621	1.060	8.920	2.922	1.784	-0.199	4.097	1.048	0.499
0.20	0.153	0.535	2.327	1.174	8.800	3.211	1.581	-0.040	3.834	0.864	0.477
0.40	0.148	0.526	2.596	1.191	8.652	3.516	1.729	-0.132	3.556	0.668	0.458
0.60	0.142	0.517	2.573	1.264	8.468	3.842	1.696	-0.093	3.257	0.457	0.439
0.80	0.134	0.509	2.538	1.346	8.235	4.199	1.657	-0.049	2.932	0.226	0.421
0.99	0.125	0.500	2.487	1.437	7.932	4.580	1.611	-0.003	2.572	0.033	0.405

(b) $\beta = \alpha / 4$

α	a_1	λ_1	d_1^R	d_1^I	N_1	S_1	$f_R\left(\frac{\ell}{D}\to 0\right)$	$f_I\left(\frac{\ell}{D}\to 0\right)$	N_f	S_f	k
-0.99	0.380	0.688	2.303	0.687	7.419	0.332	1.902	-0.006	4.894	1.380	0.774
-0.80	0.305	0.652	2.369	0.736	7.833	0.708	1.878	-0.051	4.780	1.338	0.700
-0.60	0.251	0.619	2.435	0.793	8.208	1.151	1.854	-0.094	4.642	1.285	0.635
-0.40	0.212	0.591	2.499	0.861	8.518	1.655	1.831	-0.133	4.484	1.221	0.582
-0.20	0.182	0.566	2.561	0.947	8.759	2.236	1.808	-0.168	4.305	1.146	0.537
0.00	0.157	0.545	2.621	1.060	8.920	2.922	1.784	-0.199	4.101	1.059	0.500
0.20	0.150	0.526	2.677	1.221	8.985	3.767	1.759	-0.226	3.869	0.959	0.469
0.40	0.143	0.511	2.730	1.474	8.922	4.904	1.733	-0.247	3.604	0.845	0.446
0.60	0.139	0.501	2.780	1.972	8.667	6.784	1.702	-0.261	3.299	0.714	0.432
0.80	0.138	0.508	2.902	4.126	7.934	13.72	1.666	-0.266	2.943	0.562	0.454

Figure Captions

Figure 1. (a) A circular cylindrical pillar of material 1 is attached to a half-space of material 2, with a remote tensile stress σ^{∞} applied to the top of the pillar; (b) the tensile traction on the interface is limited to the value σ_c, and this is treated as a cohesive zone of length ℓ from the interface corner. The problem shown in (b) is solved by superposition of two problems (c) and (d). When the cohesive zone lies within the zone of dominance of the corner singularity, the problems for (c) and (d) reduce to the asymptotic problems as shown in (e) and (f), respectively.

Figure 2. An interfacial crack of length *c* with a crack tip process zone of uniform cohesive strength σ_c and length ℓ due to a corner singularity as stipulated by (1.4) for the displacement field u_j on the outer boundary.

Figure 3. Dependence of *k* upon (α, β).

Figure 4. Cohesive zone length as a function of the remote stress for selected values of α, with (a) $\beta = 0$ and (b) $\beta = \alpha / 4$. Free sliding is allowed in the cohesive zone. The dotted line in part (a) refers to the analytic model as given by Eq. (4.4), upon taking $b = R$.

Figure 5. Debond strength σ_F / σ_c as a function of pillar diameter D_c / δ_c for selected values of α, with (a) $\beta = 0$ and (b) $\beta = \alpha / 4$. Free sliding is allowed in the cohesive zone. The dotted line in part (a) refers to the analytic model as given by Eq. (4.4) and Eq. (4.23), upon taking $\delta(R) = \delta_c$.

Figure 6. Debond strength σ_F / σ_c as a function of the pillar diameter D_c / δ_c for selected values of α, with (a) $\beta = 0$ and (b) $\beta = \alpha / 4$. No sliding is allowed in the cohesive zone.

Figure 7. (a) Phase (i) of detachment, and (b) phase (ii) of detachment, for a rigid, frictionless pillar.

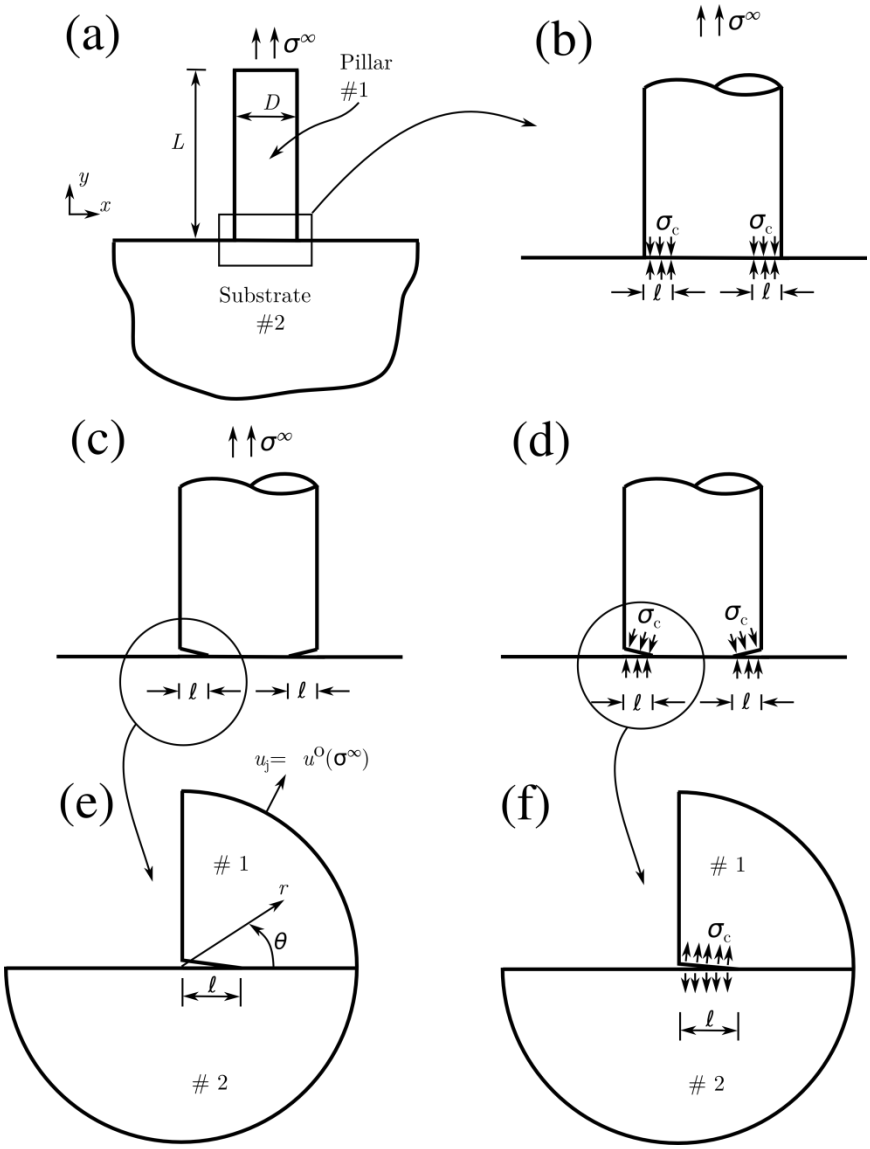

Figure 1. (a) A circular cylindrical pillar of material 1 is attached to a half-space of material 2, with a remote tensile stress σ^∞ applied to the top of the pillar; (b) the tensile traction on the interface is limited to the value σ_c, and this is treated as a cohesive zone of length ℓ from the interface corner. The problem shown in (b) is solved by superposition of two problems (c) and (d). When the cohesive zone lies within the zone of dominance of the corner singularity, the problems for (c) and (d) reduce to the asymptotic problems as shown in (e) and (f), respectively.

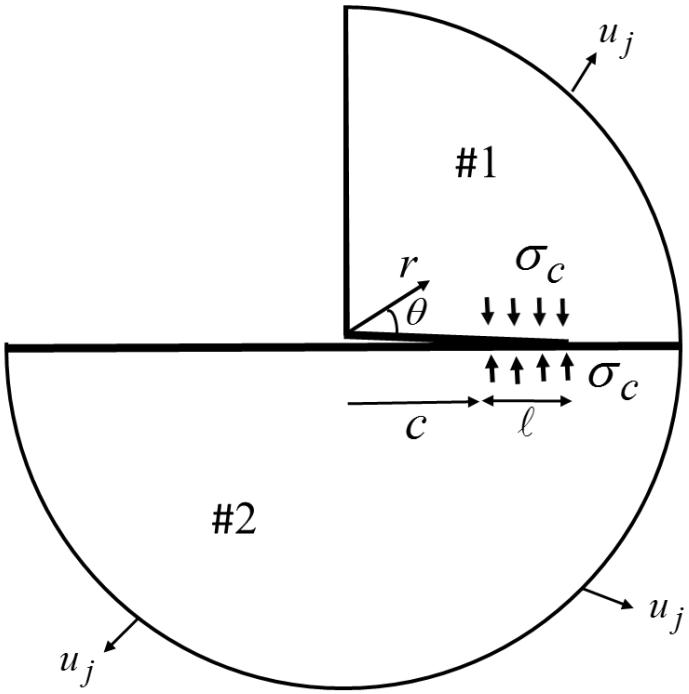

Figure 2. An interfacial crack of length c with a crack tip process zone of uniform cohesive strength σ_c and length ℓ due to a corner singularity as stipulated by (1.4) for the displacement field u_j on the outer boundary.

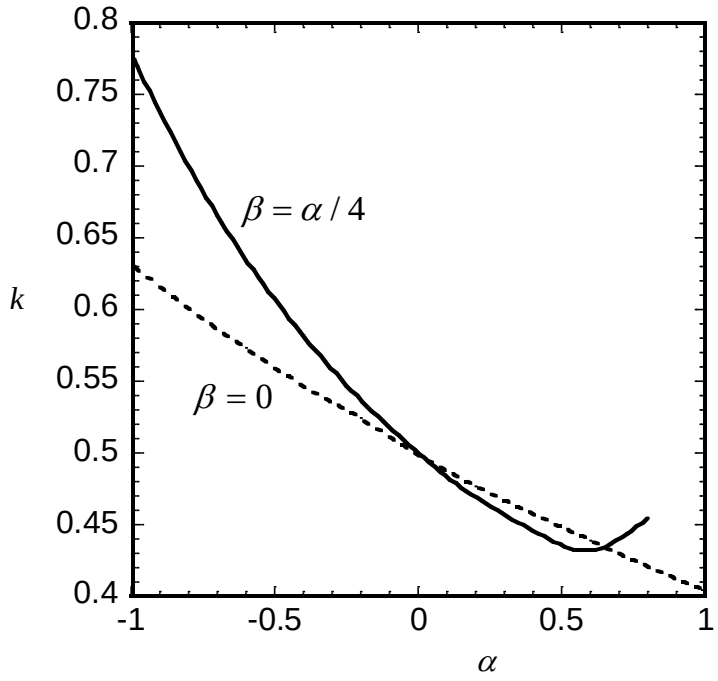

Figure 3. Dependence of k upon (α, β).

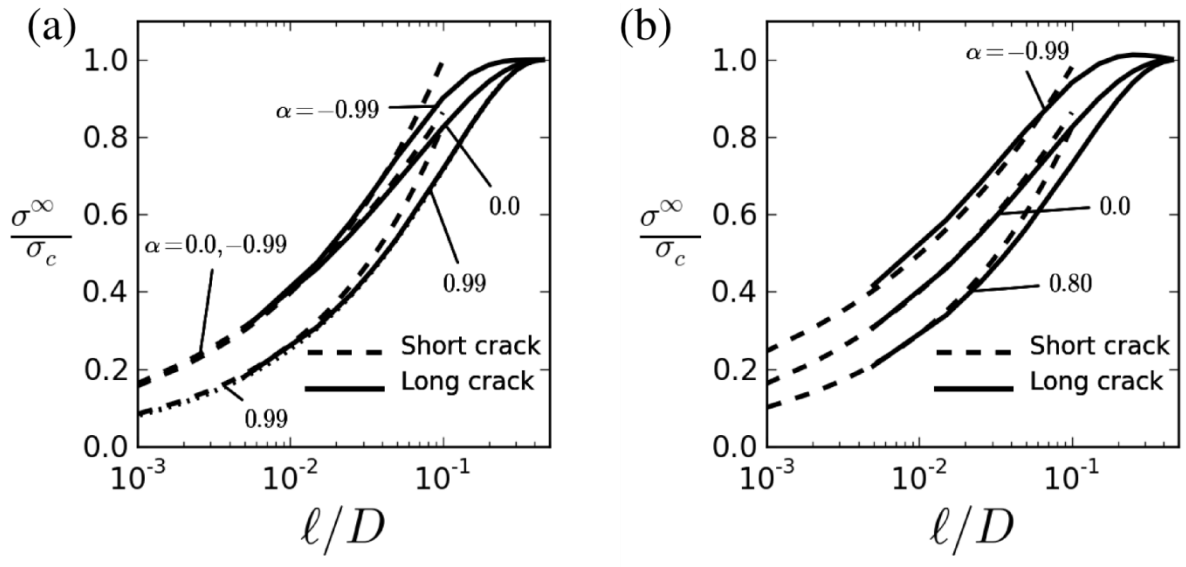

Figure 4. Cohesive zone length as a function of the remote stress for selected values of α, with (a) $\beta=0$ and (b) $\beta=\alpha/4$. Free sliding is allowed in the cohesive zone. The dotted line in part (a) refers to the analytic model as given by Eq. (4.4), upon taking $b=R$.

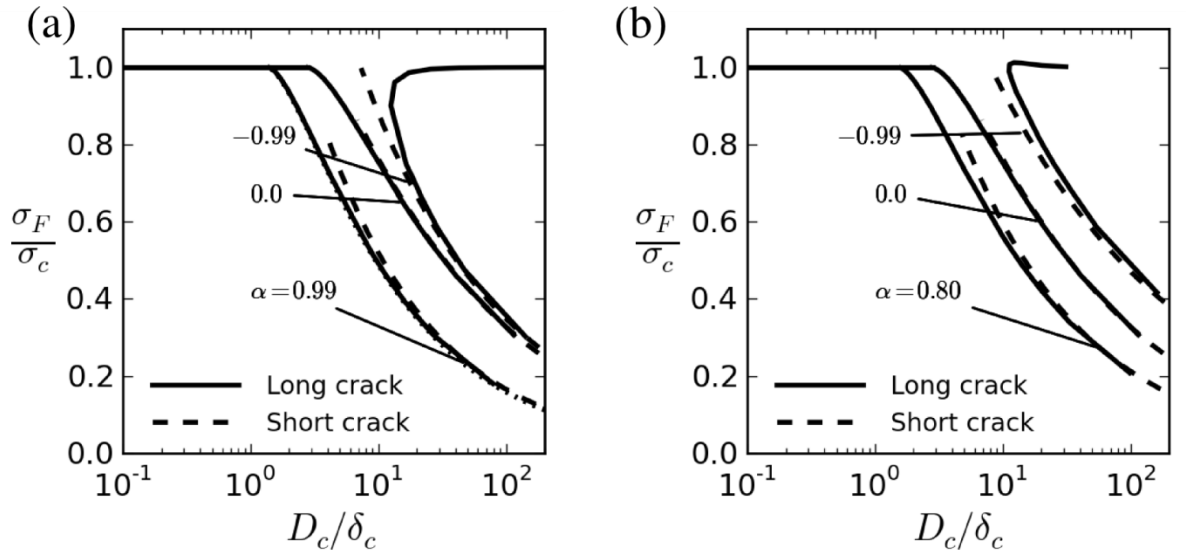

Figure 5. Debond strength σ_F/σ_c as a function of pillar diameter D_c/δ_c for selected values of α, with (a) $\beta=0$ and (b) $\beta=\alpha/4$. Free sliding is allowed in the cohesive zone. The dotted line in part (a) refers to the analytic model as given by Eq. (4.4) and Eq. (4.23), upon taking $\delta(R)=\delta_c$.

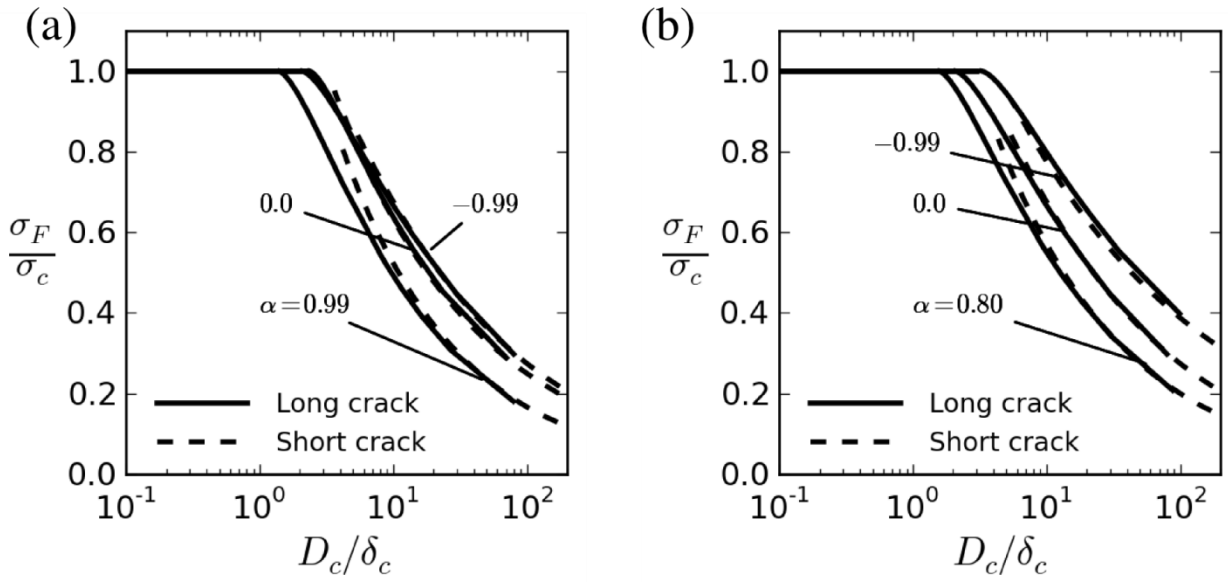

Figure 6. Debond strength σ_F / σ_c as a function of the pillar diameter D_c / δ_c for selected values of α, with (a) $\beta = 0$ and (b) $\beta = \alpha / 4$. No sliding is allowed in the cohesive zone.

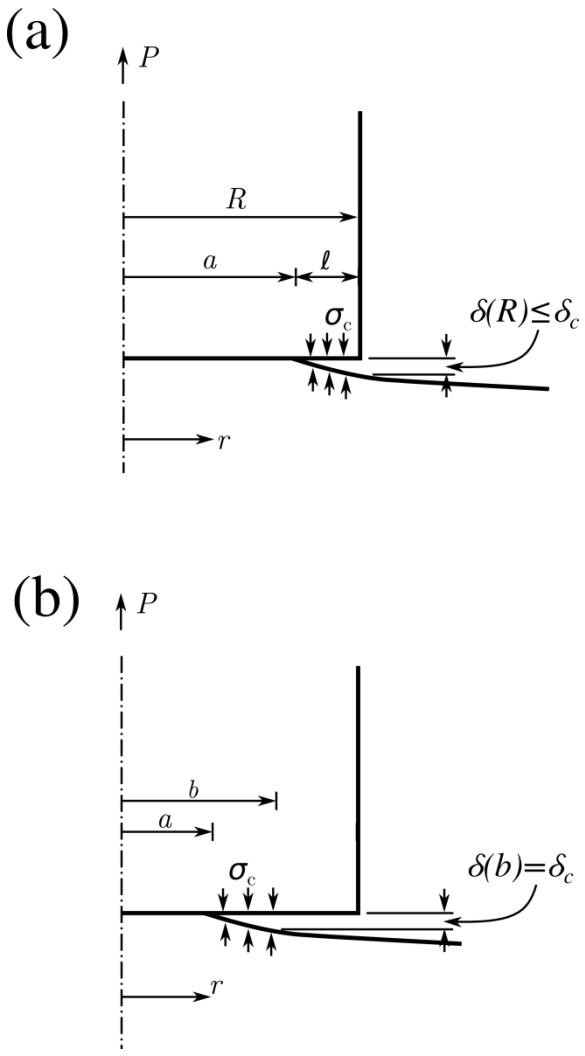

Figure 7. (a) Phase (i) of detachment, and (b) phase (ii) of detachment, for a rigid, frictionless pillar.